Acta Mech 235, 3149–3166 (2024)
https://doi.org/10.1007/s00707-023-03840-8

ORIGINAL PAPER

Ali Najafi Ardekany · **Zohreh Malek Hosseini**

Boundary controllability of a nonlinear elastic body

Received: 27 August 2023 / Revised: 11 December 2023 / Accepted: 13 December 2023 / Published online: 2 March 2024

Abstract This paper addresses the exact controllability of vibrations in a three-dimensional Cosserat elastic solid body using mathematical techniques such as operator theory and semigroup methods. The verification of exact (shape) controllability is accomplished through the application of the Hilbert Uniqueness Method, which involves investigating the boundary observability for the dual system. In partial differential equations control theory, the concept of exact observability for the dual system is fundamental to achieving exact controllability, although it differs from the common understanding of controllability. While control theory for systems governed by ordinary differential equations (ODEs) has a relatively formal and standardized approach, systems with distributed parameters, such as the Cosserat medium under consideration, involve a multitude of technical inequalities that must be established. Notably, Cosserat media possess six degrees of freedom for microstructures, in contrast to classical media with only three degrees of freedom. Consequently, exact control is required for all six variables, encompassing three translational and three rotational degrees of freedom, while classical media only necessitate the exact control of three translational variables. The paper concludes with a series of numerical studies utilizing the fast Fourier transform (FFT) and various simulations, which serve to validate the effectiveness of the proposed control scheme.

1 Introduction

Flexible structures, as infinite-dimensional systems, play a vital role in science and technology. Examples of these structures include strings, beams, plates, and shells, which are encountered in various mechanical engineering applications. To model these continuous systems, partial differential equations (PDEs) along with a set of boundary conditions (BCs) are used., However, due to the mathematical complexities of these PDE models, most researchers employ discretization techniques to transform the governing PDEs into a set of Ordinary Differential Equations for solving vibration and control problems in these complex systems [1, 2].

For instance, in the context of suppression vibrations in beams, as seen in reference [3], the governing PDE of an Euler–Bernoulli beam was converted into a set of ODEs using the Galerkin method and finite element method, respectively. Subsequently, a controller was designed for the resulting ODE model to control the undesirable vibration of the system. Unfortunately, the stability theorem derived for an ODE model cannot be directly applied to the original PDE model. In fact, the neglected effects of the omitted frequencies and mode shapes could potentially lead to the destabilization of the mechanical system under a discretized model-based controller (referred to as spillover instability).

A. N. Ardekany (✉) · Z. M. Hosseini
Faculty of Mechanical Engineering, K. N. Toosi University of Technology, Tehran, Iran
e-mail: najafi@kntu.ac.ir

Z. M. Hosseini
e-mail: z.malekhoseini@email.kntu.ac.ir

To address the issue of control spillover, boundary control strategies have been proposed for PDE models of flexible systems. In the context of distributed parameter system, the placement of actuators/sensors at boundaries is crucial. This approach is favored because boundary sensing and boundary actuating are more practical and less challenging to implement compared to using actuators and sensors distributed within the domain itself [4, 5]. Consequently, many studies have focused on concepts such as boundary controllability and boundary stabilization. It is worth nothing that for the non-distributed parameter systems (ODE systems), the concepts of controllability and observability lead to standard methods with related theorems that can be readily verified without significant difficulty. However, for distributed parameter systems, this is not necessarily the case.

From a practical perspective, the problem of the exact controllability for the infinite-dimensional systems has garnered considerable attention from researchers. Exact controllability entails the ability to control the shape of an infinite-dimensional system governed by Partial Differential Equations (PDEs) [6]. In the context of mechanical flexible structures, it involves to selecting appropriate boundary that enable one to guide the system to a desired shape and desired velocity profile within a finite time. For instance, in the case of a string, the states of the system are defined by the position and velocity of each material point of the string. Therefore, exact controllability implies steering all points of the string to their intended desired positions and velocities whitin finite time. It should be noted that, as demonstrated by Dolecki and Russell [7], the concept of exact observability for an infinite-dimensional system is related to the exact controllability of the dual system. In the field of exact controllability, the survey paper authored by Lagnese [8] and the comprehensive exposition by Bensoussan [9] provide extensive findings.

In many engineering applications involving flexible and elastic structures, the presence of a high-performance controller is essential for system improvement. Consequently, many studies have been conducted in the realm of vibration control of these systems, leveraging the concepts of boundary control and exact controllability. For instance, in reference [10], an adaptive boundary control method is proposed to mitigate the vibration of a flexible marine riser system in the presence of ocean current disturbance. In this research, the riser system is modeled as a classical Euler–Bernoulli cantilever structure. Boundary control and exact controllability have also been applied to control microstructures. Vatankhah et al. investigate boundary stabilization and exact controllability of Euler–Bernoulli micro-beams, modeled using strain gradient theory, through a straightforward boundary control law in [6]. [5], Najafi et al. utilize the boundary control method to stabilize undesired vibration in a composite material. In a separate research endover [11], they adress the boundary stabilization problem for a three-dimensional elastic Cosserat body. In the applied problem context, Entessari et al. explore the intricate challenge of gantry crane stabilization [12]. Furthermore, an interesting work focuces on the shape control of a composite plate using piezoelectric materials [13]. This research examines exact controllability through the use of distributed actuators and sensors.

In many researches, experimental observations have demonstrated the suitability of Cosserat elasticity theory for enhanced modeling of composite materials, microstructures,and other applications[13]. In the Cosserat theory, infinitesimal particles are endowed with micro-rotations, which means that each particle possesses directors. The field equations formulated using the Cosserat model encompass a broader range of physical phenomenon and can account for the results of classical mechanics as well [15]. Unlike classical elasticity, which permits only three translations (in 3D) for particles, Cosserat theory endows each particle, which no only three translations but also three independent micro-rotations, without without any requirement for these rotations to be accompanied by translations. This unique property enable Cosserat elasticity to address a wide spectrum of phenomena, including crack propagations, blood modeling and porous media.

Certain studies provide an analytical analysis of the propagation of a semi-infinite crack within a pre-stressed functionally graded orthotropic strip (FGOS) exposed to horizontally polarized shear wave propagation. The analytical tools employed for this analysis include the Wiener–Hopf technique and two-sided Fourier integral transforms. These techniques are applied to solve the model, leading to the derivation of a closed-form expression for the stress intensity factor (SIF) corresponding to a constant intensity force (CF). The study explores the impact of various parameters, such as crack speed, crack length, horizontal compressive pre-stress/horizontal tensile pre-stress, vertical compressive pre-stress/vertical tensile pre-stress, functional gradient parameter, and anisotropy parameter, on the SIF within a pre-stressed FGOS. This examination is carried out through numerical computations and graphical representations. Furthermore, for the sake of validation, the results obtained for CF under constant load conditions are compared with those established in previous studies as a special case of the problem [16–18].

Lie et al. [19] explored an industrially relevant scenario involving an axially moving accelerated string subject to input saturation and external disturbances. Their primary goal was to minimize vibration offsets, and

they achieved this through a boundary control approach. To address input saturation constrains, an auxiliary term was introduced. Moreover, they employed both finite-dimensional and infinite-dimensional observers to handle unknown disturbances. Notably, their control strategy addresses the existence, uniqueness, and convergence of the solution for the closed-loop string system without relying on model reduction techniques. Through simulations, they demonstrated the effectiveness of their chosen control method, substantiated by the appropriate selection of control parameters.

Reference [20] delves into fluid boundary control applied to composite shell vibrations that involve partial fluid filling. These vibrations are governed by linear boundary control regulations, which encompass forces and moments exerted at the boundaries of the composite shell. Notably, this study achieves boundary stabilization without the need for actuators within the domain, using the fluid's free surface for the purpose. The study demonstrates boundary stabilization through the utilization of semigroup techniques and the LaSalle invariant set theory.

In other research endeavors, the behavior of a moving Griffith crack within an initially stressed isotropic strip with infinite length and finite thickness is scrutinized. The strip is subjected to moving parallel punches of constant load at its boundaries, due to plane wave propagation under point loading. The formulation of this model incorporates coupled singular integral equations and singularities of the Cauchy type. The analysis of point loads located at the moving crack edge employs the Dirac delta function, while the Hilbert transformation properties are harnessed to determine the stress intensity factor (SIF) in the presence of constant point loading. To assess the impact of various parameters, such as initial stresses, punch pressure, distinct positions of point load, length, and speed of the crack, numerical simulations and graphical representations are conducted for the isotropic material strip under consideration, as detailed in references [21] and [22].

The study by Dimitri et al. [23] focuses on evaluating the suitability of a rock formation, particularly the kaolinite-rich Opalinus Clay, for hosting radioactive waste. They treat this sedimentary rock as a transversely isotropic geomaterial. Using the eXtended Finite Element Method (XFEM), the research investigates the formation and propagation of cracks within the rock specimen. Notably, it examines the influence of different notch dimensions and scale effects on the rock's response to fracturing, particularly regarding its peak load-bearing capacity. The study utilizes XFEM results to develop an analytical formulation that approximates the material's response in terms of load and crack mouth opening displacement. This formulation provides reliable estimates of the peak load value and time history response, which are compared to experimental data from existing literature. The analytical model offers valuable insights for various design purposes.

The study explores the behavior of a Griffith crack in a transversely isotropic dry sandy strip. The crack is affected by mechanical point loading due to propagating plane waves and applied through moving parallel punch pressure on the layer's surface. Using a model based on coupled singular integral equations and the Dirac delta function, the research derives the stress intensity factor (SIF) for constant point loading. The study comprehensively analyzes how parameters like crack length, speed, punch pressure, sandiness, and point load positions impact the SIF for both transversely isotropic dry sandy materials and isotropic material strips. A comparative investigation of the SIF is carried out for different scenarios, emphasizing key aspects of the problem [24].

Singh et al. analyzed the behavior of a semi-infinite crack in a pre-stressed magnetoelastic orthotropic strip subjected to SH-wave propagation. Using the Wiener–Hopf method and Fourier integral transforms, they derived a closed-form solution for the stress intensity factor under a constant concentrated force. The study investigated the influence of factors like crack length, speed, magnetoelastic properties, and pre-stress on the stress intensity factor. Comparisons were made with a pre-stressed magnetoelastic isotropic strip, revealing the distinct characteristics and the role of orthotropy. This research highlights the significant impact of magnetoelasticity and pre-stress on crack propagation in orthotropic elastic materials, contributing to structural analysis, material durability assessment, and the understanding of engineering failures [25].

In this paper, the problem of the exact controllability of the three-dimensional elastic Cosserat body is examined. The controllability problems of lumped- parameter systems, which are characterized by ordinary differential equations as their governing equations, are regarded as special cases within the realm of exact controllability for infinite-dimensional systems.

Extending solutions from lumped systems to infinite-dimensional systems introduces inherent challenges. As expounded in this paper, various technical obstacles must be surmounted to achieve the intended objectives. These hurdles encompass the utilization of appropriate technical inequalities, the establishment of a suitable Hilbert space, and the adaptation of the boundary controllability problem into a boundary observability problem for the dual system, all within the context of the inner product space associated with the Hilbert space. Notably, a similar problem was explored for classical elastic bodies by Alabau and Komornik [23]. The task

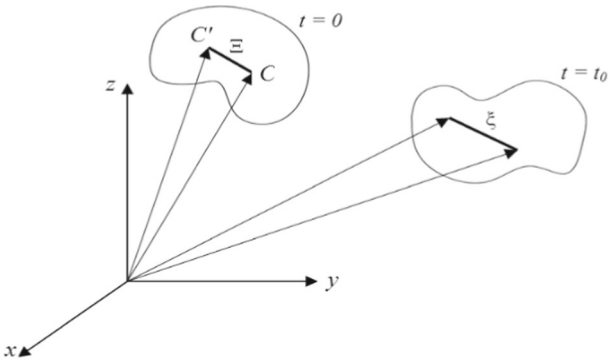

Fig. 1 Deformation of a cosserat element

of performing simulation runs to address controllability, particularly for shape control, in the context of three-dimensional elastic structures is inherently intricate. While there is an abundance of simulations available for lumped systems, there have been relatively few contributions dealing with the complexities of exact boundary controllability for such intricate systems.

In this research, simulation were conducted to validate the theoretical results of a specific Cosserat system.

The primary focus of this study revolved around achieving precise controllability for the governing partial differential equation (PDE) associated with a Cosserat elastic body, specifically through the implementation of boundary actions. The use of boundary actuators offered significant practical advantages, particularly from an engineering perspective, as it allowed for the exclusive use of actuators placed along the boundaries, eliminating the need for in-domain actuators. Moreover, the design of control strategies based on discretizing the PDE model could result in spillover instabilities. These instabilities become apparent when control design is executed for the finite-dimensional model of the system.

The structure of this paper is as follows: In Sect. 2, the governing equations are presented along with their visual representations. Section 3 is dedicated to the study of the exact controllability problem using the Hilbert Uniqueness Method. In Sect. 4, numerical simulations are included to validate the analytical results, and finally, Sect. 5 presents the conclusion of the paper.

2 Three-dimensonal cosserat elastic: equations of the motion

The governing equations of the Cosserat elastic continua are specified by the following set of linear Partial Differential Equations (PDEs) (where notation ∇ stand for the Divergence operator).

$$\begin{aligned}&(\lambda+\mu)\nabla(\nabla.\boldsymbol{u})+(\mu+\kappa)\nabla^2\boldsymbol{u}+\kappa\nabla\times\boldsymbol{\varphi}+\rho\boldsymbol{f}=\rho\ddot{\boldsymbol{u}}\quad \text{in } \Omega\times(0,T)\\&(\alpha+\beta)\nabla(\nabla.\boldsymbol{\varphi})+\gamma\nabla^2\boldsymbol{\varphi}+\kappa\nabla\times\boldsymbol{u}-2\kappa\boldsymbol{\varphi}+\rho\boldsymbol{l}=\rho j\ddot{\boldsymbol{\varphi}}\quad \text{in } \Omega\times(0,T)\end{aligned}\tag{1}$$

Ω is a region that is bounded and has a smooth boundary encompassing the Cosserat elastic media, $\boldsymbol{u}$ represents for the displacement vector ($\dot{\boldsymbol{u}}$ is the time derivative of $\boldsymbol{u}$) and $\boldsymbol{\varphi}$ denotes the microrotation vector. Additionally,α, β and γ are the new constants described in the Cosserat elasticity and the coefficients λ and μ are Lame's constants ρ and j are positive constants representing the mass density and micro inertia, respectively [27]. Finally, $\boldsymbol{f}$ and $\boldsymbol{l}$ stand for the external force and moment vectors. For closer examination Fig. 1 illustrates the characteristics of the Cosserat micro element, which can undergo micro-elongation the micro-rotations.

In the context of the Cosserat elastic body, it is important to note that, in the general case, there are a minimum of three directors associated with each micro-element. The following equation outlines the relevant boundary conditions.

$$\begin{cases}u=0,\varphi=0\,at\,\Gamma_1\\ \boldsymbol{t}_n=\boldsymbol{m}_n=0\,at\,\Gamma_2=\Gamma-\Gamma_1\end{cases}\tag{2}$$

where Γ denotes the boundary of the body, Γ_1 stands for the clamped portion of the boundary and Γ_2 corresponds to the free part of the boundary. The equations for stress and couple stress at the boundaries are as follows [28].

$$\boldsymbol{t}_n=\lambda(\nabla.\boldsymbol{u})\boldsymbol{n}+(\mu+\kappa)(\boldsymbol{n}.\nabla)\boldsymbol{u}+\mu\nabla(\boldsymbol{n}.\boldsymbol{u})+\kappa\boldsymbol{n}\times\varphi \text{ on } \Gamma_2\times(0,T)\tag{3}$$

$$\boldsymbol{m}_n = \alpha(\nabla.\varphi)\boldsymbol{n} + \beta(\boldsymbol{n}.\nabla)\varphi + \gamma\nabla(\boldsymbol{n}.\varphi) \text{ in } \Gamma_2 \times (0,T) \tag{4}$$

Here **n** denotes the unit outward normal to the boundary. It crucial to emphasize that Eqs. (3) and (4) are applicable exclusively to Γ_2[27].

3 Exact controllability of the three-dimensional cosserat elastic media

The energy of the Cosserat body is described as follows:

$$\begin{aligned} E = \frac{1}{2}\iiint_{\Omega}\Big\{&\lambda(\nabla.\boldsymbol{x}_1)(\nabla.\boldsymbol{x}_1) + (\mu+\kappa)\ \mathrm{tr}\,[(\nabla\mathbf{x}_1)^T(\nabla\boldsymbol{x}_1)] - \kappa\boldsymbol{x}_3.\nabla\times\boldsymbol{x}_1 + 2\kappa\boldsymbol{x}_3.\boldsymbol{x}_3 \\ &- \kappa\boldsymbol{x}_3.\nabla\times\boldsymbol{x}_1 + \mu\ \mathrm{tr}[(\nabla\mathbf{x}_1)(\nabla\boldsymbol{x}_1)] + \alpha(\nabla.x_3)(\nabla.x_3) + \gamma\mathrm{tr}[(\nabla\mathbf{x}_3)^T(\nabla x_3)] \\ &+\beta\mathrm{tr}[(\nabla\mathbf{x}_3)(\nabla x_3)] + \rho x_2.x_2 + \rho j x_4.x_4\}d\Omega \end{aligned} \tag{5}$$

For the sake of simplicity and without loss of generality, we assume $\rho = \rho j = 1$, whereas

$$(\boldsymbol{u},\boldsymbol{\varphi}) \in \mathbb{H} = \{(\boldsymbol{u},\boldsymbol{\varphi}) \in \boldsymbol{H}^2(\Omega)\times\boldsymbol{H}^2(\Omega) : \boldsymbol{u}|_\Gamma = \boldsymbol{\varphi}|_\Gamma = 0\} \tag{6}$$

Given that the energy of the body cannot be negative, it follows that $E \geq 0$. It is assumed that the domain Ω is

$$\Omega = \{\boldsymbol{x} \in \mathbb{R}^3 : |\boldsymbol{x}| < R\} \tag{7}$$

Here $\mathbb{R}$ represents the set of real numbers.

Theorem 1 *Assuming that T is arbitrarily large but sufficient, the solutions of the following equation satisfy the relation (9).*

$$\begin{cases} \dot{\boldsymbol{X}} = \boldsymbol{A}\boldsymbol{X} \\ \boldsymbol{x}_1 = \boldsymbol{x}_2 = \boldsymbol{x}_3 = \boldsymbol{x}_4 = 0 \ \ in\ \ \Gamma \\ \boldsymbol{X}_0 \in (\boldsymbol{H}_0^1(\Omega))^4 \bigcap \left(H^2(\Omega)\right)^4 \end{cases} \tag{8}$$

$$(2T/(1+\zeta) - \chi)E \leq R\int_0^T\int_\Gamma \Sigma d\Gamma dt \leq ((4\zeta+2)/(1+\zeta) + \chi)E \tag{9}$$

where

$$H^1{}_0(\Omega) = \left(H^1{}_0(\Omega)\right)^3 and H^2(\Omega) = \left(H^2(\Omega)\right)^3 \tag{10}$$

Furthermore, ζ and χ are positive real numbers, and Σ is the trace of the potential energy on the boundary. The potential energy of the Cosserat body is described as follows:

$$\begin{aligned} Potential\,Energy = 1/2\iiint_{\Omega}\Big\{&\lambda(\nabla.\boldsymbol{x}_1)(\nabla.\boldsymbol{x}_1) + (\mu+\kappa)tr[(\nabla\boldsymbol{x}_1)^T(\nabla\boldsymbol{x}_1)] \\ &+ 2\kappa\boldsymbol{x}_3.\boldsymbol{x}_3 - \kappa\boldsymbol{x}_3.\nabla\times\boldsymbol{x}_1 - \kappa\boldsymbol{x}_1.\nabla\times\boldsymbol{x}_3 + \mu tr[(\nabla\boldsymbol{x}_1)(\nabla\boldsymbol{x}_1)] + \alpha(\nabla.\boldsymbol{x}_3)(\nabla.\boldsymbol{x}_3) \\ &+\gamma tr[(\nabla\boldsymbol{x}_3)^T(\nabla\boldsymbol{x}_3)] + \beta tr[(\nabla\boldsymbol{x}_3)(\nabla\boldsymbol{x}_3)]\Big\}d\Omega \end{aligned} \tag{11}$$

To complete the proof of the above theorem, the definitions of the stress and the couple stress tensors are adopted.

Definition The stress tensor t_{ij} and couple stress tensor m_{ij} can be defined as follows: [28],

$$t_{ij} = \lambda \varepsilon_{mm} \delta_{ij} + (\mu + \kappa)\varepsilon_{ij} + \mu \varepsilon_{ji} \tag{12}$$

$$m_{ij} = \alpha \gamma_{mm} \delta_{ij} + \beta \gamma_{ij} + \gamma \gamma_{ij} \tag{13}$$

Here, ε_{ijk} represents the classical permutation symbol and δ_{ij} stands for the Kronecker delta. Additionally, the following equations apply to ε_{ij} and γ_{ij}

$$\varepsilon_{ij} = u_{j,i} + \varepsilon_{jik}\varphi_k \tag{14}$$

$$\gamma_{ij} = \varphi_{i,j} \tag{15}$$

where $r = x$ in $\mathbb{R}^3$ and $\boldsymbol{n} = (n_1, n_2, n_3)$ represents the unit normal vector to Γ. By multiplying Eq. (1) by $r_m u_{i,m}$ and then integrating by parts, a result is obtained:

$$\int_o^T \int_\Gamma [2Ru_{i,j} t_{ij} + R\dot{u}_i \dot{u}_i] d\Gamma dt = \left[\int_\Omega 2r_m u_{i,m} \dot{u}_i \right]_0^T + \int_0^T \int_\Omega [2u_{i,j} t_{ji} + 3\dot{u}_i \dot{u}_i + 2r_m t_{ji} u_{i,jm}] d\Omega dt \tag{16}$$

Pursuing the same procedure as for Eq. (2) yields the following relations

$$\left[\int_\Omega \dot{u}_i u_i \right]_0^T + \int_0^T \int_\Omega [u_{i,j} t_{ji} - \dot{u}_i \dot{u}_i] d\Omega dt = 0 \tag{17}$$

$$\int_0^T \int_\Gamma R(\varphi_{i,j} m_{ji} + \dot{\varphi}_i \dot{\varphi}_i) d\Gamma dt = \left[\int_\Omega 2r_m \varphi_{i,m} \dot{\varphi}_i d\Omega \right]_0^T + \int_0^T \int_\Omega [3\dot{\varphi}_i \dot{\varphi}_i - m_{ji}\varphi_{i,j}] d\Omega dt + \int_0^T \int_\Omega [2r_m t_{ji} \varphi_{l,m} \varepsilon_{lij}] d\Omega dt \tag{18}$$

And

$$\int_\Omega \varphi_i \dot{\varphi}_i d\Omega]_0^T + \int_0^T \int_\Omega (\varphi_{i,j} m_{ji} - \dot{\varphi}_i \dot{\varphi}_i) d\Omega dt + \int_0^T \int_\Omega (\varphi_i \varepsilon_{ipq} t_{qp}) d\Omega dt = 0 \tag{19}$$

By adding Eqs. (16), (17), (18) and (19) with appropriate coefficients, and then applying the boundary conditions, the following relation will be obtained

$$\int_0^T \int_\Gamma R(\varphi_{i,j} m_{ji} + 2u_{i,j} t_{ji}) d\Gamma dt = \left\{ \int_\Omega [2r_m(\varphi_{i,m} \dot{\varphi}_i + u_{i,m} \dot{u}_i) + 2u_i \dot{u}_i + 2\varphi_i \dot{\varphi}_i] d\Omega \right\}_0^T + \int_0^T \int_\Omega (\varphi_{i,j} m_{ji} + \dot{\varphi}_i \dot{\varphi}_i + \dot{u}_i \dot{u}_i + 4t_{ji}\varepsilon_{ji}) d\Omega dt - \int_0^T \int_\Omega (2\varphi_i \varepsilon_{ipq} t_{qp} + 3t_{ji}\varepsilon_{ji}) d\Omega dt + \int_0^T \int_\Gamma R t_{ji} \varepsilon_{ji} d\Gamma dt \tag{20}$$

Rearranging terms in the integrals yields

$$\int_0^T \int_\Gamma R(\varphi_{i,j} m_{ji} + 2u_{i,j} t_{ji} - t_{ji}\varepsilon_{ji}) d\Gamma dt = \left\{ \int_\Omega [(2r_m \varphi_{i,m} + 2\varphi_i)\dot{\varphi}_i + (2r_m u_{i,m} + u_i)\dot{u}_i] d\Omega \right\}_0^T + 2ET - \int_0^T \int_\Omega 2\varphi_i \varepsilon_{ipq} t_{qp} d\Omega dt \tag{21}$$

The fact that the total energy of the elastic body can be reformulated in the following form has been utilized in the aforementioned relation [28].

$$E = 1/2 \int_\Omega (\varphi_{i,j} m_{ji} + \dot{\varphi}_i \dot{\varphi}_i + \dot{u}_i \dot{u}_i + t_{ji}\varepsilon_{ji}) d\Omega \tag{22}$$

The focus of this step is on the term "$2\varphi_i \varepsilon_{ipq} t_{qp}$". Initially, one may consider.

$$A = 2\varphi_i \varepsilon_{ipq} t_{qp} = -2\kappa \boldsymbol{\varphi}.\nabla \times \boldsymbol{u} + 4\kappa \boldsymbol{\varphi}.\boldsymbol{\varphi} \tag{23}$$

Before proceeding with the reminder of the proof, it is necessary to determine the upper bound of the aforementioned term.

$$\begin{aligned} |-2\kappa\varphi.\nabla \times \boldsymbol{u} + 4\kappa\varphi.\varphi| &\le |2\kappa\varphi.\nabla \times \boldsymbol{u}| + |4\kappa\varphi.\varphi| \le \kappa|\nabla \times \boldsymbol{u}|^2 + \kappa|\varphi.\varphi| + 4\kappa|\varphi.\varphi| \\ &\le 2\kappa \ \mathrm{tr}[(\nabla \mathbf{u})^T(\nabla \boldsymbol{u})] + 5\kappa \ \mathrm{tr}[(\nabla\varphi)^T(\nabla\varphi)] \\ &= 2\kappa \ \mathrm{tr}[(\nabla \mathbf{u})^T(\nabla \boldsymbol{u})] + 5\kappa/(\gamma-\beta)(\gamma-\beta)\mathrm{tr}[(\nabla\varphi)^T(\nabla\varphi)] \\ &\le \max\{2, 5\kappa/(\gamma-\beta)\}\{\kappa \ \mathrm{tr}[(\nabla \mathbf{u})^T(\nabla \boldsymbol{u})] + (\gamma-\beta)\mathrm{tr}[(\nabla\varphi)^T(\nabla\varphi)]\}dt \end{aligned} \tag{24}$$

To establish the algebraic relation mentioned above, the relation (25) has been used

$$|\nabla \times \boldsymbol{u}|^2 = \ \mathrm{tr}\,[(\nabla \mathbf{u})^T(\nabla \boldsymbol{u})] - \mathrm{tr}\,[(\nabla \mathbf{u})(\nabla \mathbf{u})] \tag{25}$$

accustoming

$$C = \kappa tr[(\nabla \boldsymbol{u})^T(\nabla \boldsymbol{u})] + (\gamma-\beta)tr[(\nabla \boldsymbol{\varphi})^T(\nabla \boldsymbol{\varphi})] \tag{26}$$

and

$$\zeta = \ \max\{2, 5\kappa/(\gamma-\beta)\} \tag{27}$$

one can obtain

$$|A| \le 2\zeta/(1+\zeta)E \tag{28}$$

Therefore, the following relation is obtained

$$\begin{aligned} \left|2ET - \int_0^T \int_\Gamma R(\varphi_i, {}_j m_{ji} + 2u_i, {}_j t_{ji} - t_{ji}\varepsilon_{ji})d\Gamma dt\right| \le \left\{\int_\Omega [(2r_m\varphi_i, {}_m + 2\varphi_i)\dot{\varphi}_i + (2r_m u_i, {}_m + 2u_i)\dot{u}_i]d\Omega\right\}_0^T \\ + 2\zeta/(1+\zeta)ET \end{aligned} \tag{29}$$

The relation

$$u_i, {}_j t_{ji} = \varepsilon_{ji} t_{ji} \tag{30}$$

Is true on the boundary, so,

$$\begin{aligned} \left|2ET - \int_0^T \int_\Gamma R(\varphi_i, {}_j m_{ji} + u_i, {}_j t_{ji})d\Gamma dt\right| \le \left\{\int_\Omega [(2r_m u_i, {}_m + 2u_i)\dot{u}_i\right\}_0^T + (2r_m\varphi_i, \\ {}_m + 2\varphi_i)\dot{\varphi}_i]d\Omega + 2\zeta/(1+\zeta)ET \end{aligned} \tag{31}$$

To complete the proof, the following equation is considered

$$\|2r_m u_i, {}_m + 2u_i\|_{L^2(\Omega)} \le \|2r_m u_i, {}_m\|_{L^2(\Omega)} \tag{32}$$

This is due to the following identity

$$\begin{aligned} \|2r_m u_i, {}_m + 2u_i\|^2_{L^2(\Omega)} - \|2r_m u_i, {}_m\|^2_{L^2(\Omega)} &= \int_\Omega \left(4u_i^2 + 8r_m u_i, {}_m u_i\right)d\Omega \\ &= \int_\Omega (4u_i^2 - 12u_i^2)d\Omega + \int_\Gamma 4r_m n_m u_i^2 d\Gamma = -\int_\Omega 8u_i^2 d\Omega \end{aligned} \tag{33}$$

The analogous outcome is true for the terms φ_i's. Based on this result, the following equation can be obtained

$$\begin{aligned}
&\left|\left\{\int_\Omega [(2r_m u_{i,m} + 2u_i)\dot{u}_i + (2r_m\varphi_{i,m} + 2\varphi_i)\dot{\varphi}_i]d\Omega\right\}_0^T\right| \\
&\leq 2R\sum_i\left[\left(\int_\Omega |\nabla u_i|^2 d\Omega\right)^{\frac{1}{2}}\left(\int_\Omega (\dot{u}_i)^2 d\Omega\right)^{\frac{1}{2}}\right] + 2R\sum_i\left[\left(\int_\Omega |\nabla\varphi_i|^2 d\Omega\right)^{1/2}\left(\int_\Omega (\dot{\varphi}_i)^2 d\Omega\right)^{1/2}\right] \\
&\leq R\delta_1\int_\Omega u_{i,m}u_{i,m}d\Omega + R\delta_1^{-1}\int_\Omega \dot{u}_i\dot{u}_i d\Omega + R\delta_2\int_\Omega \varphi_{i,m}\varphi_{i,m}d\Omega + R\delta_1^{-1}\int_\Omega \dot{\varphi}_i\dot{\varphi}_i d\Omega
\end{aligned} \tag{34}$$

In order to complete the proof, additional lemmas are needed.

Lemma 1 *suppose* λ, α, μ*and*γ *are positive constants, then,*

$$a)t_{ij}\varepsilon_{ij} \geq \kappa\varepsilon_{ij}\varepsilon_{ij}b)m_{ji}\gamma_{ij} \geq (\gamma-\beta)\gamma_{ij}\gamma_{ij} \tag{35}$$

Proof Constructing $t_{ij}\varepsilon_{ij}$ yields the following result.

$$t_{ij}\varepsilon_{ij} = \lambda\varepsilon_{mm}\varepsilon_{kk} + (\mu+\kappa)\varepsilon_{ij}\varepsilon_{ij} + \mu\varepsilon_{ji}\varepsilon_{ij} \geq (\mu+\kappa)\varepsilon_{ij}\varepsilon_{ij} + \mu\varepsilon_{ji}\varepsilon_{ij} = \mu(\varepsilon_{ij}\varepsilon_{ij} + \varepsilon_{ji}\varepsilon_{ij}) + \kappa\varepsilon_{ij}\varepsilon_{ij} \geq \kappa\varepsilon_{ij}\varepsilon_{ij} \tag{36}$$

Another inequality can be obtained the same procedure.

Lemma 2 *The following inequalities hold in* Ω.

$$a)2\varepsilon_{mip}u_{i,m}\varphi_p \leq \varepsilon_{mi}\varepsilon_{mi} + 6\varphi_p\varphi_p \tag{37}$$

$$b)u_{i,m}u_{i,m} \leq 2\varepsilon_{mi}\varepsilon_{mi} + 4\varphi_i\varphi_i \tag{38}$$

$$2\varepsilon_{mip}u_{i,m}\varphi_p = 2\varphi.\nabla\times\boldsymbol{u} \leq 2|\varphi|.|\nabla\times\boldsymbol{u}| \leq 2(\varphi.\varphi)^{1/2}.(2u_{i,m}u_{i,m})^{1/2} \tag{39}$$

Proof Considering the following relation

$$\begin{aligned}
\varepsilon_{mi}\varepsilon_{mi} - 2\varphi.\nabla\times\boldsymbol{u} + 6\varphi.\varphi = u_{i,m}u_{i,m} - 4\varphi.\nabla\times\boldsymbol{u} + 8\varphi.\varphi \geq u_{i,m}u_{i,m} - 4\sqrt{2}(\varphi.\varphi)^{1/2}(u_{i,m}u_{i,m})^{1/2} \\
\geq [(u_{i,m}u_{i,m})^{1/2} - 8(\varphi.\varphi)^{1/2}]^2 \geq 0
\end{aligned} \tag{40}$$

Leads to the first inequality of the lemma 2. For the second inequality, consider the relation (41).

$$u_{i,m}u_{i,m} = \varepsilon_{mi}\varepsilon_{mi} - 2\boldsymbol{\varphi}.\boldsymbol{\varphi} + 2\boldsymbol{\varphi}.\nabla\times\boldsymbol{u} \leq \varepsilon_{mi}\varepsilon_{mi} - 2\boldsymbol{\varphi}.\boldsymbol{\varphi} + \varepsilon_{mi}\varepsilon_{mi} + 6\boldsymbol{\varphi}.\boldsymbol{\varphi} \tag{41}$$

which lasts the following inequality

$$u_{i,m}u_{i,m} \leq 2\varepsilon_{mi}\varepsilon_{mi} + 4\boldsymbol{\varphi}.\boldsymbol{\varphi} \tag{42}$$

Lemma 3 *The following inequality holds.*

$$\int_\Omega u_{i,m}u_{i,m}d\Omega \leq \int_\Omega 2\varepsilon_{mi}\varepsilon_{mi} + 4\varphi_{i,m}\varphi_{i,m}d\Omega \tag{43}$$

Proof The inequality becomes evident by utilizing the second result of Lemma 2 and applying Pioncare's inequality.

By employing the above-mentioned lemmas, Eq. (34) leads to

$$\begin{aligned}
&\left|\left[\int_\Omega \{(2r_m u_{i,m} + 2u_i)\dot{u}_i + (2r_m\varphi_{i,m} + 2\varphi_i)\dot{\varphi}_i\}d\Omega\right]_0^T\right| \\
&\leq R\delta_1\int_\Omega 2\varepsilon_{im}\varepsilon_{im} + +4\varphi_{i,m}\varphi_{i,m}]d\Omega + R\delta_1^{-1}\int_\Omega \dot{u}_i\dot{u}_i d\Omega \\
&+R\delta_2\int_\Omega \varphi_{i,m}\varphi_{i,m}d\Omega \\
&+R\delta_2^{-1}\int_\Omega \dot{\varphi}_i\dot{\varphi}_i d\Omega
\end{aligned} \tag{44}$$

which takes the following form

$$\begin{aligned}&\left|\left[\int_{\Omega}\{(2r_m u_{i,m}+2u_i)\dot{u}_i+(2r_m\varphi_{i,m}+2\varphi_i)\dot{\varphi}_i\}d\Omega\right]_0^T\right|\\&\le R\delta_1\int_{\Omega}2\varepsilon_{im}\varepsilon_{im}d\Omega+R\delta_1^{-1}\int_{\Omega}\dot{u}_i\dot{u}_i d\Omega\\&+(R\delta_2+4R\delta_1)\int_{\Omega}\varphi_{i,m}\varphi_{i,m}d\Omega+R\delta_2^{-1}\int_{\Omega}\dot{\varphi}_i\dot{\varphi}_i d\Omega\end{aligned}\tag{45}$$

and also

$$\begin{aligned}&\left|\left[\int_{\Omega}\{(2r_m u_{i,m}+2u_i)\dot{u}_i+(2r_m\varphi_{i,m}+2\varphi_i)\dot{\varphi}_i\}d\Omega\right]_0^T\right|\le R\delta_1/(\kappa/2)\int_{\Omega}k\varepsilon_{im}\varepsilon_{im}d\Omega+R\delta_2\\&+4R\delta_1/(\gamma-\beta)\int_{\Omega}(\gamma-\beta)\varphi_{i,m}\varphi_{i,m}d\Omega\\&+R\delta_1^{-1}\int_{\Omega}\dot{u}_i\dot{u}_i d\Omega+R\delta_2^{-1}\int_{\Omega}\dot{\varphi}_i\dot{\varphi}_i d\Omega\end{aligned}\tag{46}$$

Setting

$$\delta_1=\sqrt{\kappa/2}\&\delta_2=-\sqrt{2\kappa}+\sqrt{2\kappa+(\gamma-\beta)}\tag{47}$$

leads to

$$\begin{aligned}&\left|\int_{\Omega}\{(2r_m u_{i,m}+2u_i)\dot{u}_i+(2r_m\varphi_{i,m}+2\varphi_i)\dot{\varphi}_i\}d\Omega\right]_0^T\Big|\\&\le R\sqrt{\frac{2}{\kappa}}\int_{\Omega}[\kappa\varepsilon_{im}\varepsilon_{im}+\dot{u}_i\dot{u}_i]d\Omega+R(-\sqrt{2\kappa}+\sqrt{2\kappa+(\gamma-\beta)})^{-1}\\&\times\int_{\Omega}[(\gamma-\beta)\varphi_{i,m}\varphi_{i,m}+\dot{\varphi}_i\dot{\varphi}_i]d\Omega\end{aligned}\tag{48}$$

Using Lemma 1, the following result is obtained

$$\left|\left[\int_{\Omega}\{(2r_m u_{i,m}+2u_i)\dot{u}_i+(2r_m\varphi_{i,m}+2\varphi_i)\dot{\varphi}_i\}d\Omega\right]_0^T\right|\le Rmax\{\sqrt{2/\kappa},[-\sqrt{2\kappa}+\sqrt{2\kappa+(\gamma-\beta)}]^{-1}\}E=\chi E\tag{49}$$

Summarizing the results gives

$$(2T/(\zeta+1))-\chi)E\le R\int_0^T\int_{\Gamma}\Sigma d\Gamma dt\le((4\zeta+2)T/(\zeta+1)+\chi)E\tag{50}$$

So, the proof of Theorem 1 will be complete. To achieve the exact controllability objective, the following lemmas are required.

Lemma 4 *The following inequalities can be obtained on the boundary region* Γ.

$$a)\kappa t_{ij}\varepsilon_{ij}\le\sum_j\left|t_{ij}n_i\right|^2\le 27[\lambda^2+(\mu+\kappa)^2+\mu^2]\varepsilon_{ij}\varepsilon_{ij}\tag{51}$$

$$b)\,(\gamma-\beta)m_{ij}\gamma_{ij}\le\sum_i\left|m_{ij}n_j\right|^2\le 27[\alpha^2+\beta^2+\gamma^2]\gamma_{ij}\gamma_{ij}\tag{52}$$

Proof At first, the case (a) will be considered. For the right-hand side of the inequality is expressed as follows:

$$\sum_j |t_{ij}n_i|^2 \le \sum_{i,j} |t_{ij}|^2 = t_{ij}t_{ij} = \sum_{i,j}\sum_{k,l}[\lambda\delta_{kl}\delta_{ij} + (\mu+\kappa)\delta_{ik}\delta_{jl} + \mu\delta_{il}\delta_{jk}]\varepsilon_{ij}{}^2$$
$$\le \sum_{k,l} 3[\lambda^2 + (\mu+\kappa)^2 + \mu^2]\varepsilon_{ij}\varepsilon_{ij} = 27[\lambda^2 + (\mu+\kappa)^2 + \mu^2]\varepsilon_{ij}\varepsilon_{ij} \tag{53}$$

For the left-hand side of the inequality, it can be obtained

$$t_{ij}\varepsilon_{ij} = t_{ij}u_{j,i} = t_{ij}n_i u_{j,n} \le \left(\sum_j (t_{ij}n_i)^2\right)^{1/2} (u_{j,i}u_{j,i})^{1/2}$$
$$\le \left(\sum_j (t_{ij}n_i)^2\right)^{1/2} (u_{j,i}u_{j,i})^{1/2} = \left(\sum_j (t_{ij}n_i)^2\right)^{1/2} (\varepsilon_{ij}\varepsilon_{ij})^{1/2} \tag{54}$$

Applying the result of Lemma 1 yields

$$t_{ij}\varepsilon_{ij} \le \left(\sum_j (t_{ij}n_i)^2\right)^{1/2} \left(t_{ij}\varepsilon_{ij}/\kappa\right)^{1/2} \tag{55}$$

which takes the following form

$$\kappa t_{ij}\varepsilon_{ij} \le \sum_j (t_{ij}n_i)^2 \tag{56}$$

The proof for case (b) is entirely similar to the procedure described above.

Lemma 5 *Let the following set of the equations be satisfied.*

$$\begin{cases} (\lambda+\mu)\nabla(\nabla.u) + (\mu+\kappa)\nabla^2 u + \kappa\nabla\times\varphi = \ddot{\boldsymbol{u}} \\ (\alpha+\beta)\nabla(\nabla.\varphi) + \gamma\nabla^2\varphi + \kappa\nabla\times u - 2\kappa\varphi = \ddot{\boldsymbol{\varphi}} \\ u_i = 0 \quad on \quad \Gamma\times(0,T) \\ \varphi_i = 0 \quad on \quad \Gamma\times(0,T) \end{cases} \tag{57}$$

$$\begin{cases} (\lambda+\mu)\nabla(\nabla.y) + (\mu+\kappa)\nabla^2 y + \kappa\nabla\times\psi = \ddot{y} \\ (\alpha+\beta)\nabla(\nabla.\psi) + (\gamma)\nabla^2\psi + \kappa\nabla\times y - 2\kappa\psi = \ddot{\boldsymbol{\psi}} \\ y_i = v_i \ on \ \Gamma\times(0,T), \ y_i(t=T) = 0 \\ \psi_i = w_i \ on \ \Gamma\times(0,T), \psi_i(t=T) = 0 \end{cases} \tag{58}$$

It can be obtained

$$I = \int_0^T \int_\Omega [u_i(\ddot{y}_i - t_{ij,j}(\boldsymbol{y})) + \varphi_i(\ddot{\psi}_i - m_{ij,j}(\boldsymbol{\psi}) - \varepsilon_{ijk}t_{jk}(\boldsymbol{y}))]d\Omega dt$$
$$= \int_0^T \int_\Omega [y_i(\ddot{u}_i - t_{ij,j}(\boldsymbol{u})) + \psi_i(\ddot{\varphi}_i - m_{ij,j}(\varphi) - \varepsilon_{ijk}t_{jk}(\boldsymbol{u}))]d\Omega dt$$
$$+ \left\{\int_\Omega [(u_i\dot{y}_i - \dot{u}_i y_i) + (\varphi_i\dot{\psi}_i - \dot{\varphi}_i\psi_i)]d\Omega\right\}_0^T$$
$$+ \int_0^T \int_\Gamma [(t_{ij}(\boldsymbol{u})n_j y_i - t_{ij}(\boldsymbol{y})n_j u_i) + (m_{ij}(\varphi)n_j\psi_i - m_{ij}(\boldsymbol{\psi})n_j\varphi_i)]d\Gamma dt = 0 \tag{59}$$

Proof By Utilizing integrations by parts, the desired result can be achieved. Furthermore, by applying the related governing equations to the above equation, one can obtain.

$$\begin{aligned} I =& \left\{ \int_{\Omega} [(u_i \dot{y}_i - \dot{u}_i \ddot{y}_i) + (\varphi_i \dot{\psi}_i - \dot{\varphi}_i \psi_i)] d\Omega \right\}_0^T \\ &+ \int_0^T \int_{\Gamma} [(t_{ij}(\boldsymbol{u}) n_j y_i - t_{ij}(\boldsymbol{y}) n_j u_i) \\ &+ (m_{ij}(') n_j \psi_i - m_{ij}(\boldsymbol{\psi}) n_j \varphi_i)] d\Gamma dt = 0 \end{aligned} \tag{60}$$

The exact controllability is concluded is based on the following mapping (Λ) [29],

$$\Lambda(\mathcal{X}(t=0), \dot{\mathcal{X}}(t=0)) = (\dot{\mathcal{Y}}(t=0), -\mathcal{Y}(t=0)) \tag{61}$$

where $\mathcal{X} = (\boldsymbol{u}, \boldsymbol{\varphi})$, $\mathcal{Y} = (\boldsymbol{y}, \boldsymbol{\psi})$ and

$$\boldsymbol{H} = (L^2(\Omega))^3 \times (L^2(\Omega))^3 \times (H^{-1}(\Omega))^3 \times (H^{-1}(\Omega))^3 \tag{62}$$

Λ is a linear mapping. The following theorem characterizes the nature of the Λ.

Theorem 2 *Let $T \geq \chi(1+\zeta)/2$, then for any given $\boldsymbol{y}(t=0)$, $\widetilde{\mathbf{y}}_0(t=0) \in (L^2(\Omega))^3$ and*

$$\dot{\boldsymbol{y}}(t=0), \widetilde{\mathbf{y}}_1(t=0) \in (H^{-1}(\Omega))^3 \tag{63}$$

and also $\boldsymbol{\psi}(t=0)$, $\widetilde{\boldsymbol{\psi}}_0(t=0) \in (L^2(\Omega))^3$ and

$$\dot{\boldsymbol{\psi}}(t=0), \widetilde{\boldsymbol{\psi}}_1(t=0) \in (H^{-1}(\Omega))^3 \tag{64}$$

there exist $\boldsymbol{v} = (v_1, v_2, v_3)$ and $\boldsymbol{w} = (w_1, w_2, w_3)$ both belonging to $L^2_{loc}(\mathbb{R}; (L^2(\Gamma))^3)$ which the solutions of the following set of equations

$$\begin{cases} (\lambda+\mu)\nabla(\nabla.y) + (\mu+\kappa)\nabla^2 y + \kappa \nabla \times \psi = \ddot{y} \\ (\alpha+\beta)\nabla(\nabla.\psi) + \gamma \nabla^2 \psi + \kappa \nabla \times u - 2\kappa\psi = \ddot{\boldsymbol{\psi}} \\ y_i = v_i = t_{ij}(\boldsymbol{u}) n_j \ \ on \quad \Gamma \times (0,T) \\ \psi_i = w_i = m_{ij}(\boldsymbol{u}) n_j \ on \quad \Gamma \times (0,T) \end{cases} \tag{65}$$

satisfy the following conditions

$$\boldsymbol{y}(t=T) = \widetilde{\mathbf{y}}_0 \ and \ \dot{\mathbf{y}}(t=T) = \widetilde{\mathbf{y}}_1 \boldsymbol{\psi}(t=T) = \widetilde{\boldsymbol{\psi}}_0 \ and \ \dot{\boldsymbol{\psi}}(t=T) = \widetilde{\boldsymbol{\psi}}_1 \tag{66}$$

Proof To do this, one needs to assume the case where $\tilde{\mathbf{y}}_0 = \tilde{\mathbf{y}}_1 = \tilde{\boldsymbol{\psi}}_0 = \tilde{\boldsymbol{\psi}}_1$ in Ω [29, 30]. Therefore, utilizing the results of Theorem 1 and Lemmas 4 and 5 associated with HUM, it suffices to demonstrate that the mapping Λ is an isomorphism from $\boldsymbol{H}$ onto $\boldsymbol{H}'$, making the proof straightforward. To achieve this, the following inner product will be defined.

$$\boldsymbol{H} = (L^2(\Omega))^3 \times (L^2(\Omega))^3 \times (H^{-1}(\Omega))^3 \times (H^{-1}(\Omega))^3 \tag{67}$$

Onto

$$\boldsymbol{H}' = (L^2(\Omega))^3 \times (L^2(\Omega))^3 \times (H(\Omega))^3 \times (H(\Omega))^3 \tag{68}$$

With the results of Lemmas 4 and 5, one can achieve

$$\langle \Lambda(\mathcal{X}(0), \dot{\mathcal{X}}(0)), (\mathcal{X}(0), \dot{\mathcal{X}}(0)) \rangle_{\boldsymbol{H}', \boldsymbol{H}} = \int_0^T \int_{\Gamma} [(t_{ij}(\boldsymbol{u}) n_j)^2 + (m_{ij}(\varphi) n_j)^2] d\Gamma dt \tag{69}$$

By employing Lemma 5 and Theorem 1, it can be deduced that Λ is an isomorphism. Subsequently, by applying HUM, the proof of Theorem 2 will be evident.

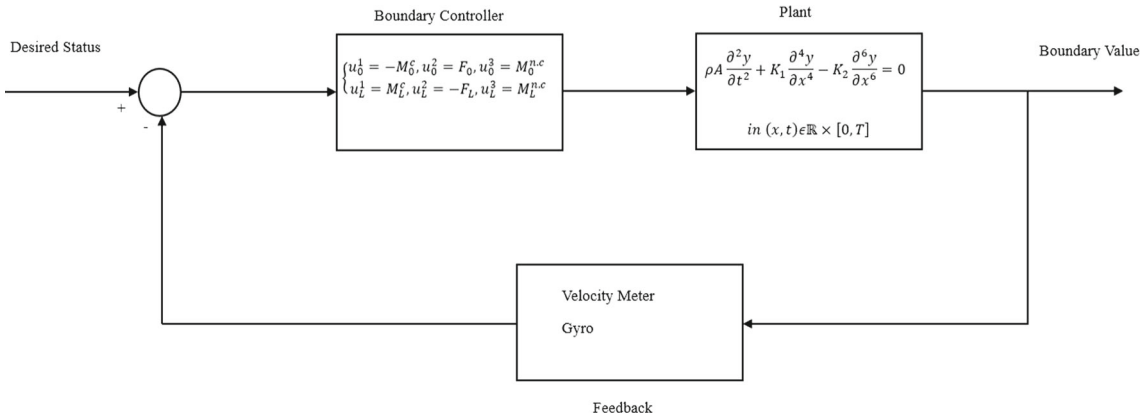

Fig. 2 Control diagram for closed-loop boundary control of an euler–bernoulli beam

4 Numerical results for a Euler–Bernoulli micro beam

In this section, numerical results for an Euler–Bernoulli microbeam with a length of L are being presented and discussed. The governing equation and boundary conditions for the microbeam are as follows:

$$\rho A \frac{\partial^2 y}{\partial t^2} + K_1 \frac{\partial^4 y}{\partial x^4} - K_2 \frac{\partial^6 y}{\partial x^6} = 0, in(x,t) \epsilon \mathbb{R} \times [0,T] \begin{cases} at\, x = 0 : \ y|_{(0,t)} = u_0^1, \ \frac{\partial y}{\partial x}\Big|_{(0,t)} = u_0^2, \ \frac{\partial^2 y}{\partial x^2}\Big|_{(0,t)} = u_0^3 \\ at\, x = L : \ y|_{(L,t)} = u_L^1, \ \frac{\partial y}{\partial x}\Big|_{(L,t)} = u_L^2, \ \frac{\partial^2 y}{\partial x^2}\Big|_{(L,t)} = u_L^3 \end{cases} \tag{70}$$

In the above relations, y represents the deflection at various points along the beam. The boundary controls at $x = 0$ and $x = L$, denotes as u_0^i and u_L^i (where $i = 1,2,3$), are defined as follows:

$$\begin{cases} u_0^1 = -M_0^c, u_0^2 = F_0, u_0^3 = M_0^{n.c} \\ u_L^1 = M_L^c, u_L^2 = -F_L, u_L^3 = M_L^{n.c} \end{cases} \tag{71}$$

In the provided context, F represents the applied force, while M^c and $M^{n.c}$ represent the moments.

$$\begin{cases} F_{0,L} = K_2 \frac{\partial^5 y}{\partial x^5} - K_1 \frac{\partial^3 y}{\partial x^3} \\ M_{0,L}^c = K_1 \frac{\partial^2 y}{\partial x^2} - K_2 \frac{\partial^4 y}{\partial x^4} \\ M_{0,L}^{n.c} = K_2 \frac{\partial^3 y}{\partial x^3} \end{cases} \tag{72}$$

The control diagram for closed-loop boundary control of an euler–bernoulli beam is shown in Fig. 2.

To demonstrate the exact controllability of non-classical Euler–Bernoulli microbeams, it is essential to conduct numerical simulations on the system using control inputs. In various studies, the numerical solution to the problem of exact controllability is consistently noted as a challenging task in the realm of partial differential equations. This challenge arises due to the limitations of conventional methods, such as finite element analysis or finite difference methods, which are extensively employed for simulating partial differential equations. Unfortunately, these traditional techniques often prove inadequate when applied to exact controllability problems due to their tendency toward numerical instability in this specific context. Therefore, alternative approaches and specialized numerical methods are typically required to effectively address the numerical simulation of exact controllability in systems like non-classical Euler–Bernoulli microbeams.

A novel approach for numerically solving the exact controllability problem of partial differential equations has been introduced in previous studies [32, 33]. This method is centered around the formulation of initial conditions for the system within the real number space $\mathbb{R}$, followed by the resolving of the resulting Cauchy problem through the utilization of the Fast Fourier Transform (FFT) technique. The FFT is a computational

algorithm that efficiently computes the Discrete Fourier Transform (DFT) of a sequence of numbers. It serves as a versatile tool with applications in various fields. In signal processing, it is used for analyzing and manipulating audio and image signals, facilitating tasks such as filtering and detecting specific frequency components. In image processing, it aids in converting images between time and frequency domains, assisting in various image manipulation tasks. Communication systems benefit from FFT by allowing the analysis of signal spectra, bandwidth, and modulation techniques in telecommunications.

In structural analysis, FFT is employed to identify vibration modes and frequencies in structures, bridges, and mechanical systems. It is also essential in control systems analysis, where it evaluates how systems respond to different frequencies. Additionally, the FFT finds uses in non-destructive testing (NDT) for signal analysis and flaw detection. In earthquake engineering, it is utilized to analyze seismic data, providing insights into earthquake characteristics. Overall, the FFT is a powerful and versatile tool with a wide range of applications in science and engineering [34].

One of the standout advantages of this method is its simplicity, along with its ability to address various challenges in the field of exact controllability for partial differential equations. Notably, in a separate research article [35], this method has been effectively utilized to achieve the precise controllability for a simple and classical two-dimensional Euler–Bernoulli beam, demonstrating its practical efficacy.

First stage In this initial stage, a non-classical Euler–Bernoulli microbeam characterized by infinite length, with the spatial range of x spanning from negative infinity to positive infinity $x \in (-\infty, +\infty)$ is being examined. To address this, the initial conditions of the target system are expanded within the real number space $\mathbb{R}$. The subsequent expression illustrates that, in this scenario, the initial conditions are formulated within the domain of $x \in (0, -\infty) \cup (L, +\infty)$, where their values are set to zero. Additionally, the initial conditions within the range of $0 \le x \le L$ are modeled as sinusoidal functions.

$$\rho A\frac{\partial^2\bar{\varphi}}{\partial t^2} + K_1\frac{\partial^4\bar{\varphi}}{\partial x^4} - K_2\frac{\partial^6\bar{\varphi}}{\partial x^6} = 0, in(x,t)\varepsilon\mathbb{R}\times[0,T]\begin{cases}\bar{\varphi}|_{t=0} = \begin{cases} L\left(sin\left(\frac{\pi x}{L}\right)\right)\ 0 \le x \le L \\ 0\ x\ 0, x\ L\end{cases} \\ \bar{\varphi}_{,t}\big|_{t=0} = 0\ x\varepsilon\mathbb{R}\end{cases} \tag{73}$$

Next, the modified system (73) is solved using the dependent variable $\overline{\varphi}(x, t)$, which represents the displacement of the hypothesized microbeam with infinite length. This solution is achieved through the application of the fast Fourier transform. Upon applying the Fourier transform to Eq. (73), the result is as follows:

$$\begin{aligned}\left[\rho A\frac{\partial^2\overline{\varphi}}{\partial t^2} + K_1\frac{\partial^4\overline{\varphi}}{\partial x^4} - K_2\frac{\partial^6\overline{\varphi}}{\partial x^6}\right] &= \rho A\tilde{\varphi}\left(\ddot{k},t\right) + K_1k^4\tilde{\varphi}(k,t) - K_2k^6\tilde{\varphi}(k,t) \Rightarrow \tilde{\varphi}(k,t) \\ &= \mathbb{F}[\overline{\varphi}(x,t)] = \mathbb{F}\left[\overline{\varphi}|_{t=0}\right]\cos\left(k^2\sqrt{\frac{K_1+K_2k^2}{\rho A}}t\right)\end{aligned} \tag{74}$$

The system's response (73) can be described by using the inverse Fourier transform, which results in $\overline{\varphi}(x, t) = \mathbb{F}^{-1}[\tilde{\varphi}(k, t)]$. According to the provided equation, the outcome of this inverse transformation can be represented as follows:

$$\begin{aligned}\overline{\varphi}(x,t) &= \overline{\varphi}|_{t=0} * \mathbb{F}^{-1}\left[cos\left(k^2\sqrt{\frac{K_1+K_2k^2}{\rho A}}t\right)\right] \\ &= \overline{\varphi}|_{t=0} * \left[\frac{1}{2\pi}\int_{-\infty}^{+\infty} cos\left(k^2\sqrt{\frac{K_1+K_2k^2}{\rho A}}t\right)\exp(jkx)dk\right] \\ &= \overline{\varphi}|_{t=0} * \left[\frac{1}{\pi}\int_{0}^{+\infty} cos\left(k^2\sqrt{\frac{K_1+K_2k^2}{\rho A}}t\right)\cos(kx)dk\right]\end{aligned} \tag{75}$$

Here, the notation $f * g$ represents the convolution of two functions, f and g, and $j = \sqrt{-1}$. By substituting the provided relationship, the above equation can be reformulated in the following manner:

$$\overline{\varphi}(x,t) = \frac{1}{\pi}\int_{-\infty}^{+\infty}\int_{0}^{+\infty}\overline{\varphi}(\xi)|_{t=0}cos\left(k^2\sqrt{\frac{K_1+K_2k^2}{\rho A}}t\right)\cos(k(x-\xi))dkd\xi$$
$$= \frac{1}{\pi}\int_{0}^{+1}\int_{0}^{+\infty}L\left(sin\left(\frac{\pi\xi}{L}\right)-0.5\right)cos\left(k^2\sqrt{\frac{K_1+K_2k^2}{\rho A}}t\right)\cos(k(x-\xi))dkd\xi \tag{76}$$

By confining the obtained solution $\overline{\varphi}(x,\ t)$ to the spatial domain of $x\epsilon[0,\ L]$ and the temporal domain of $t\epsilon[0,\ T]$, the function $\varphi = \overline{\varphi}|_{[0,\,L]\times[0,\,T]}$ can be regarded as the solution to the problem. This solution adheres to the specified boundary conditions and initial value, which are outlined as follows:

$$\rho A\frac{\partial^2\bar{\varphi}}{\partial t^2} + K_1\frac{\partial^4\bar{\varphi}}{\partial x^4} - K_2\frac{\partial^6\bar{\varphi}}{\partial x^6} = 0, in(x,t)\varepsilon[0,L]\times[0,T]$$
$$\begin{cases} \varphi|_{x=0,L} = \bar{\varphi}|_{x=0,L},\ \frac{\partial\varphi}{\partial x}\Big|_{x=0,L} = \frac{\partial\bar{\varphi}}{\partial x}\Big|_{x=0,L},\ \frac{\partial^2\varphi}{\partial x^2}\Big|_{x=0,L} = \frac{\partial^2\bar{\varphi}}{\partial x^2}\Big|_{x=0,L} & 0\le t\le T \\ \varphi|_{t=0} = L\left(sin\left(\frac{\pi\xi}{L}\right)-0.5\right) & 0\le x\le L \\ \varphi_{,t}\big|_{t=0} = 0 & 0\le x\le L \end{cases} \tag{77}$$

Second stage In this phase, the procedure carried out in the initial stage is replicated precisely for the function $\overline{\psi}$ (similarly to $\overline{\varphi}$) In this phase, the procedure carried out in the initial stage is replicated precisely for the function $\boldsymbol{\psi}$ (akin to φ), with the distinction that the initial conditions for the equation involving $\overline{\psi}$ are derived from the subsequent equation:

$$\begin{cases} \overline{\psi}\big|_{t=0} = \begin{cases} -\varphi(T)\ 0\le x\le L \\ 0\ x<0, x>L \end{cases} \\ \overline{\psi}_{,t}\big|_{t=0} = \begin{cases} \varphi_{,t}(T)\ 0\le x\le L \\ 0\ x<0, x>L \end{cases} \end{cases} \tag{78}$$

Following the application of the Fourier transform and subsequently the inverse Fourier transform to the governing equation of $\overline{\psi}(x,\ t)$, the resulting function can be obtained manually. In a manner analogous to the first step's treatment of the function φ, the same process is applied to the function $\boldsymbol{\psi}$, resulting in the expression $\psi = \overline{\psi}\big|_{[0,\,L]\times[0,\,T]}$. *Third stage* Now, if we take into account the subsequent relationship for the new function $z(x,\ t)$, which can be expressed as:

$$\mathrm{z(x,t)} = \varphi(x,t) + \psi(x, T-t) \tag{79}$$

Subsequently, leveraging the linearity of the operator inherent in the governing partial equation, this function will indeed constitute the solution to the problem, given the specified initial value and final value conditions.

$$\rho A\frac{\partial^2 z}{\partial t^2} + K_1\frac{\partial^4 z}{\partial x^4} - K_2\frac{\partial^6 z}{\partial x^6} = 0, in(x,t)\varepsilon[0,L]\times[0,T]$$
$$\begin{cases} z|_{x=0,L} = \varphi(x,t)|_{x=0,L} + \psi(x,T-t)|_{x=0,L}\ 0\le t\le T \\ \frac{\partial z}{\partial x}\big|_{x=0,L} = \frac{\partial\varphi}{\partial x}(x,t)\Big|_{x=0,L} + \frac{\partial\psi}{\partial x}(x,T-t)\Big|_{x=0,L}\ 0\le t\le T \\ \frac{\partial^2 z}{\partial x^2}\Big|_{x=0,L} = \frac{\partial^2\varphi}{\partial x^2}(x,t)\Big|_{x=0,L} = \frac{\partial^2\psi}{\partial x^2}(x,T-t)\Big|_{x=0,L}\ 0\le t\le T \end{cases} \tag{80}$$
$$\begin{cases} z|_{t=0} = L\left(sin\left(\frac{\pi x}{L}\right)-0.5\right)+\psi(T)\ 0\le x\le L \\ z_{,t}\big|_{t=0} = -\psi_{,t}(T)\ 0\le x\le L \end{cases}$$
$$\begin{cases} z|_{t=0} = 0\ 0\le x\le L \\ z_{,t}\big|_{t=0} = 0\ 0\le x\le L \end{cases}$$

Indeed, the variable $z(x,\ t)$ governed by the aforementioned equations bears similarity to the displacement of a non-classical Euler–Bernoulli double-free microbeam. his similarity extends to the imposition of inputs

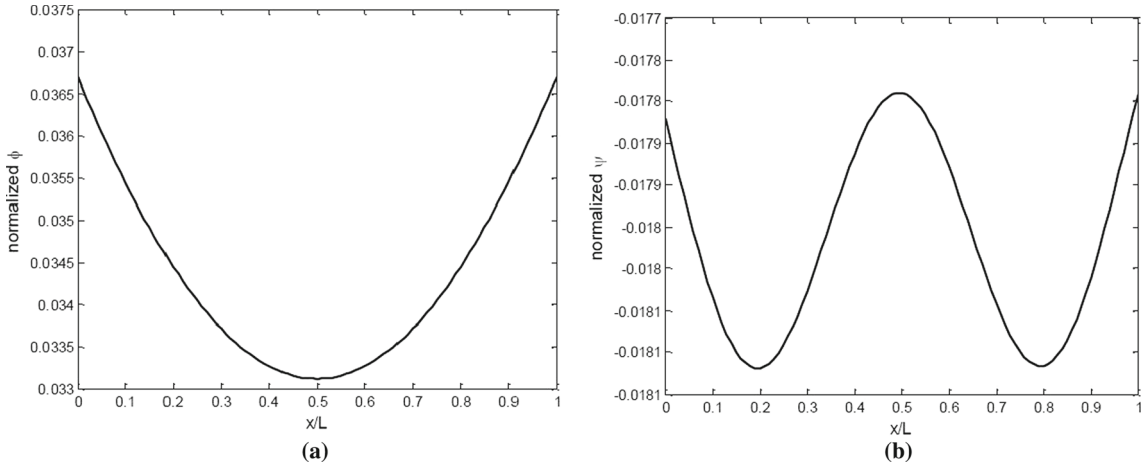

Fig. 3 Change of **a** dimensionless $\boldsymbol{\varphi}$ and **b** dimensionless $\boldsymbol{\psi}$ in length of beam (L)

$z|_{x=0,L}$, $\partial z/\partial x\big|_{x=0,L}$ and $\partial^2 z/\partial x^2\big|_{x=0,L}$ *at its initial and final boundaries. By satisfying the conditions* $z|_{t=T} = 0$ and $z_{,t}\big|_{t=T} = 0$ across the entire length domain $0 \le x \le L$, the variable $z(x, t)$ fulfills the prerequisites for exact controllability. Through the derivation of functions $\varphi(x, t)$ and $\psi(x, t)$ from the fast Fourier transform during the first and second steps of the numerical solution process, the function $z(x, t)$ and the corresponding control inputs are effectively simulated. In essence, the system of Eqs. (80), much like the system of (70), operates under the influence of control inputs (71). By numerically solving the system of Eqs. (80) using the derived functions φ and ψ, the simulation successfully addresses the exact controllability problem of the given system.

$$\widetilde{x} = x/L, \widetilde{w} = w/L, \widetilde{t} = t/L^2\sqrt{(EI)/(\rho A)}, \widetilde{F} = FL^2/(EI), \widetilde{M} = ML/(EI) \tag{81}$$

where the superscript " ~ " stands for the dimensionless variables. In addition, F and M are the boundary control force and moment feedback. For the exact controllability, an arbitrary initial condition has been assigned to the beam and the results of exact controllability are as follows:

5 Conclusion

This study introduces a comprehensive and innovative approach that address the challenging problem of exact boundary controllability in the vibrational dynamics of a three-dimensional Cosserat elastic body. To achieve this objective, the intricates of achieving boundary exact controllability were systematically explored, with the Hilbert Uniqueness Method (HUM) serving as a key analytical tool. This effort involved rigorous mathematical examinations, requiring the establishment of a series of complex technical inequalities, each of which was rigorously proven (Figs. 3, 4, 5 and 6).

To bridge the gap between theory and practical application, a numerical investigation was conducted, utilizing the powerful fast Fourier transform (FFT) technique. This numerical analysis was complemented by a series of simulations focused on a specific scenario involving a Euler–Bernoulli microbeam. These simulations were essential not only validating the theoretical results derived but also for providing concrete evidence of the feasibility and effectiveness of the proposed method.

In essence, this study not only expands our understanding of exact boundary controllability within the realm of complex vibrational systems but also underscores the crucial role that advanced mathematical techniques and numerical simulations play in connecting theory with real-world applicability.

The primary advantage of this method lies in its ability to precisely control the displacement profile of every point on the body, ensuring it conforms to the desired profile. Additionally, it concurrently adjusts the velocity profile of all points to match the desired velocity profile. This dual capability is unmatched by any other existing approach, allowing for the simultaneous manipulation of both displacement and velocity profiles. Furthermore, this method achieves this control within a finite timeframe, offering the added benefit of time-efficient steering.

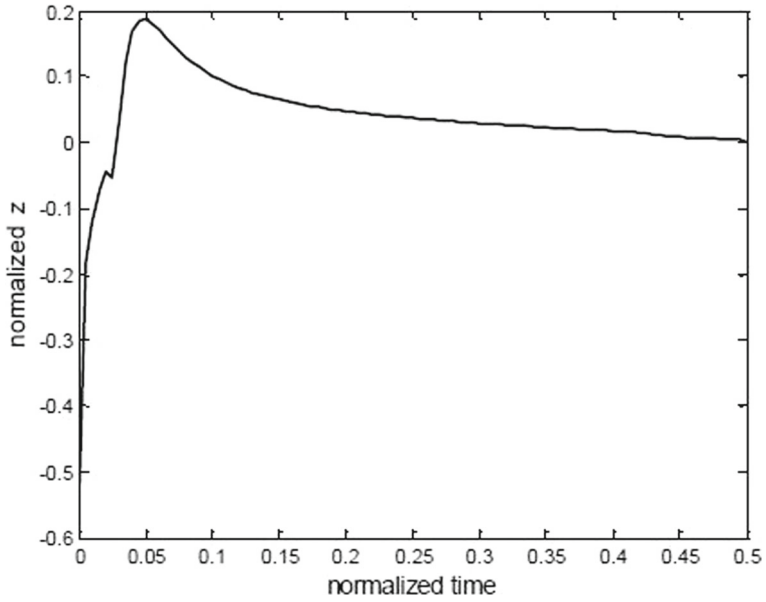

Fig. 4 Change in dimensionless deflection in free end of Euler–Bernoulli beam in exact controllability

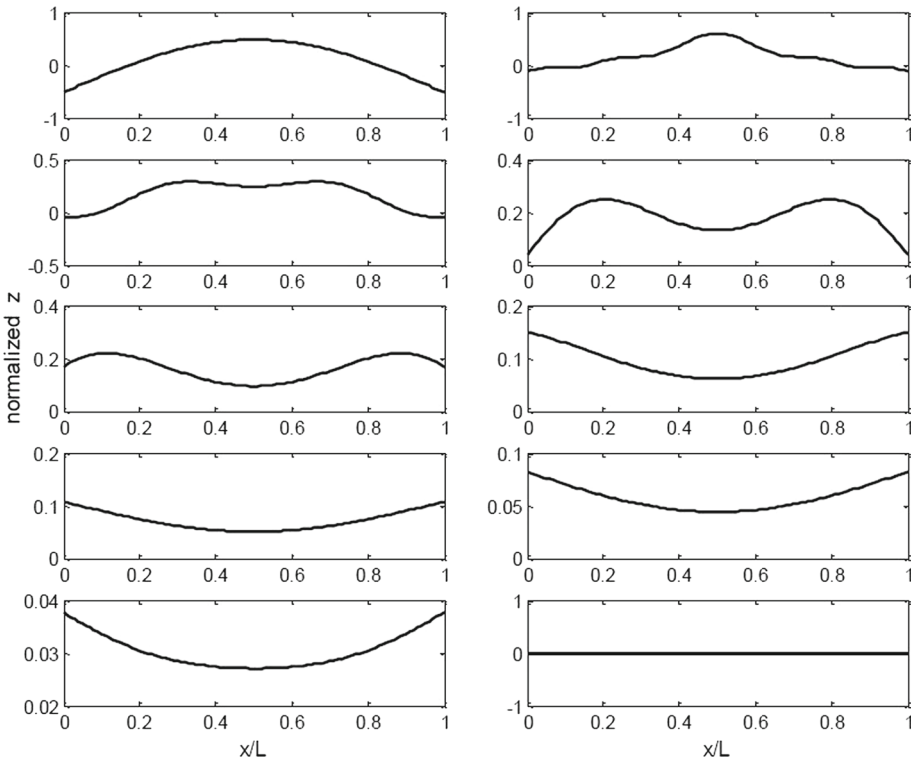

Fig. 5 2D Diagrams of dimensionless deflection of micro beam in difference points at difference times in exact controllability problem

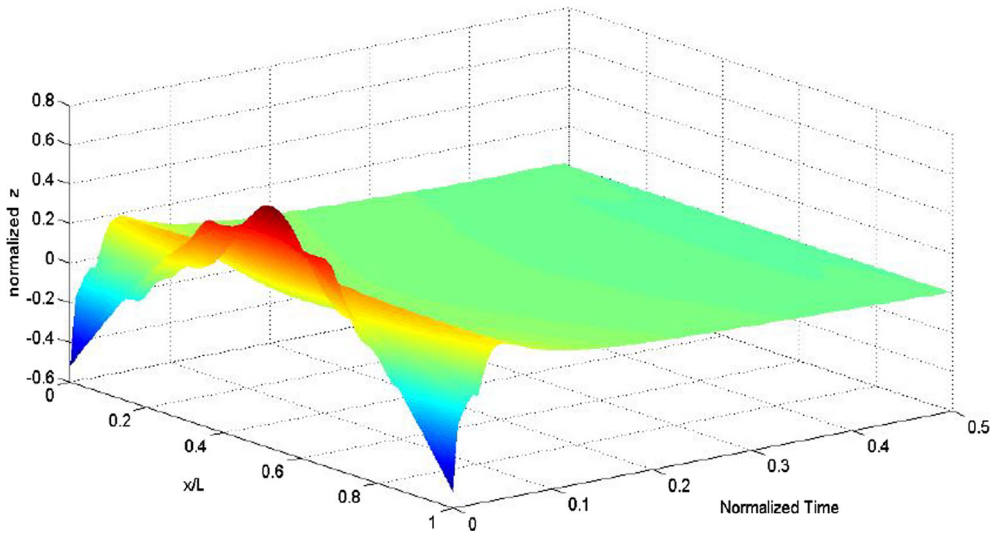

Fig. 6 3D Diagrams of dimensionless deflection of micro beam in difference points at difference times in exact controllability problem

Funding No funding was received for conducting this study.

Declarations

Conflict of interest The authors have no relevant financial or non-financial interests to disclose.

References

1. Lotfazar, A., Eghtesad, M., Najafi, A., A.: Vibration control and trajectory tracking for general in-plane motion of an Euler-Bernoulli beam via two-time scale and boundary control methods. J. Vib. Acoust. **130**(5), 51009 (2008). https://doi.org/10.1016/j.jmaa.2014.03.012
2. Najafi Ardekany, A., Daneshmand, F., Mehrvarz, A.: Vibration analysis of a micropolar membrane in contact with fluid. Iran. J. Sci. Technol. Trans. Mech. Eng. (2018). https://doi.org/10.1007/s40997-018-0188-3
3. Yu, Y., Zhang, X.N., Xie, S.L.: Optimal shape control of a beam using piezoelectric actuators with low control voltage. Smart Mater. Struct. (2009). https://doi.org/10.1088/0964-1726/18/9/095006
4. Krstic, M., Smyshlyaev, A.: Boundary Control of PDEs: A Course on Backstepping Designs. Society for Industrial and Applied Mathematics. SIAM, Philadelphia (2008)
5. Najafi, A., Eghtesad, M., Daneshmand, F.: Asymptotic stabilization of vibrating composite plates. Syst. Control Lett. **59**, 530–535 (2010)
6. Vatankhah, R., Najafi, A., Salarieh, H., Alasty, A.: Exact boundary controllability of vibrating non-classical Euler-Bernoulli micro-scale beams. J. Math. Anal. Appl. **418**, 985–997 (2014). https://doi.org/10.1016/j.jmaa.2014.03.012
7. Dolecki, S., Russell, D.: A general theory of observation and control. SIAM J. Control. Optim. **15**, 185–220 (1977). https://doi.org/10.1137/0315015
8. Lagnese J. E.: The hilbert uniqueness method: A Retrospective—from Optimal Control of Partial Differential Equations, pp.158-181, Springer, Berlin, Heidelberg (2006) https://doi.org/10.1007/BFb0043222
9. Bensoussan, A.: On the general theory of exact controllability for skew symmetric operators. Acta Appl. Math. **20**, 197–229 (1990). https://doi.org/10.1007/BF00049568
10. He, W., Ge, S.S., How, B.V.E., Choo, Y.S., Hong, K.S.: Robust adaptive boundary control of a flexible marine riser with vessel dynamics. Automatica **47**, 722–732 (2011). https://doi.org/10.1016/j.automatica.2011.01.064
11. Najafi, A., Alasty, A., Vatankhah, R., Eghtesad, M., Daneshmand, F.: Boundary Stabilization of a cosserat elastic body. Asian J. Control **19**, 2219–2225 (2017). https://doi.org/10.1002/asjc.1572
12. Entessari, F., Najafi Ardekany, A., Alasty, A.: Boundary control of a vertical nonlinear flexible manipulator considering disturbance observer and deflection constraint with torque and boundary force feedback signals. Int. J. Syst. Sci. (2021). https://doi.org/10.1080/00207721.2021.1971793
13. Plotnikova, S.V., Kulikov, G.M.: Shape control of composite plates with distributed piezoelectric actuators in a three-dimensional formulation. Mech. Compos. Mater. **56**, 557–572 (2020)
14. Kumar, R., Partap, G.: Rayleigh lamb waves in micropolar isoteropic elastic plate. Appl. Math. Mech. **27**(8), 1049–1059 (2006). https://doi.org/10.1007/s10483-006-0805-z
15. Eringen, A.C.: Microcontinuum Field Theories I: Foundations and Solids. Springer-Verlag, New York (1999)
16. Singh, A.B., Singh, A.K., Guha, S., Kummar, D.: Analysis on the propagation of crack in a functionally graded orthotropic strip under pre-stress. Waves Random Complex Media (2022). https://doi.org/10.1080/17455030.2022.2048128

17. Singh, A.K., Singh, A.K., Yadav, R.P.: Stress intensity factor of dynamic crack in double-Layered dry sandy elastic medium due to shear wave under different loading conditions. Int. J. Geomech. (2020). https://doi.org/10.1061/(ASCE)GM.1943-5622.0001827
18. Singh, A.K., Singh, A.K.: Dynamic stress concentration os a smooth moving punch influenced by a shear wave in an initially stressed dry sandy layer. Acta Mech. **233**, 1757–1768 (2022). https://doi.org/10.1007/s00707-022-03197-4
19. Liu, Y., Guo, F., He, X., Hui, Q.: Boundary control for an axially moving system with input restriction based on disturbance observers. IEEE Transact. Syst. Man Cybern. Syst. (2019). https://doi.org/10.1109/TSMC.2018.2843523
20. Liu, Y., Chen, X., Mei, Y., Wu, Y.: Observer-based boundary control for an asymmetric output-constrained flexible robotic manipulator. Sci. China Inf. Sci. (2022). https://doi.org/10.1007/s11432-019-2893-y
21. Singh, A.K., Singh, A.K.: Mathematical study on the propagation of Griffith crack in a dry sandy subjected to punch pressure. Waves Random Complex Media (2022). https://doi.org/10.1080/15397734.2023.2258196
22. Singh, A.K., Singh, A.K., Guha, A., Kumar, D.: Mathematical analysis on the propagation of Griffith crack in ana initially stressed strip subjected to punch pressure. Mech. Based Des. Struct. Mach. (2023). https://doi.org/10.1080/15397734.2023.2223614
23. Dimitri, R., Rinaldi, M., Trullo, M.: Theoretical and computational investigation of the fracturing behavior of anisotropic geomaterials. Continuum Mech. Thermodyn. **35**, 1417–1432 (2023). https://doi.org/10.1007/s00161-022-01141-4
24. Singh, A.K., Singh, A.K., Kaushik, S.K.: On analytical study of Griffith crack propagation in a transversely isotropic dry sandy punch pressured strip. Phys. Scr. (2023). https://doi.org/10.1088/1402-4896/acef6d
25. Singh, A.K., Singh, A.K., Yadav, R.P.: Analytical study on the propagation of semi-infinite crack due to SH-wave in pre-stressed magnetoelastic orthotropic strip. Mech. Based Des. Struct. Mach. (2023). https://doi.org/10.1080/15397734.2023.2258196
26. Alabau, F., Komornik, V.: Boundary observability, controllability, and stabilization of linear elastodynamic systems. SIAM J. Control. Optim. **37**(2), 521–542 (1999). https://doi.org/10.1137/S03630129963138
27. Eringen, A.C.: Continuum Physics, v. 4., 1st Edition, Elsevier Science, (1976)
28. Eringen, A.C.: Microcontinuum Field Theories I: Foundations and Solids, no, vol. 1. Springer, Heidelberg (2002)
29. Lions, L.L.: Contrôlabilité exacte, perturbations et stabilisation de systèmes distribués: Contrôlabilité exacte. Masson, (1988)
30. Komornik, V.: Exact controllability and stabilization: the multiplier method. the University of Michigan, Wiley, (1994)
31. Asghari, M., Kahrobaiyan, M.H., Rahaeifard, M., Ahmadian, M.T.: Investigation of the size effects in Timoshenko beams based on the couple stress theory. Arch. Appl. Mech. **81**, 7863–7874 (2011). https://doi.org/10.1007/s00419-010-0452-5
32. Pedregal, P., Preiago, F., Villena, J.: A numerical method of local energy decay for the boundary controllability of time-reversible distributed parameter systems. Stud. Appl. Math. **121**, 27–47 (2008). https://doi.org/10.1111/j.1467-9590.2008.00406.x
33. Pedregal, P., Preiago, F.: Some remarks on homogenization and exact boundary controllability for the one- dimensional wave equation. Q. Appl. Math. **64**, 529–546 (2006). https://doi.org/10.1090/S0033-569X-06-01022-4
34. Walker, J.S.: Fast fourier transforms,2nd Edition, Chicago, (1996)
35. Font, R., Preiago, F.: Numerical simulation of the boundary exact control for the system of linear elasticity. Appl. Math. Lett. **23**, 1021–1026 (2010). https://doi.org/10.1016/j.aml.2010.04.030